The ASAS-SN catalogue of variable stars – V. Variables in the Southern hemisphere

T. Jayasinghe [1,2]★ K. Z. Stanek,[1,2] C. S. Kochanek,[1,2] B. J. Shappee,[3]
T. W. -S. Holoien [4] T. A. Thompson,[1,2,5] J. L. Prieto,[6,7] S. Dong,[8] M. Pawlak,[9]
O. Pejcha [9] J. V. Shields,[1] G. Pojmanski,[10] S. Otero,[11] N. Hurst,[12] C. A. Britt[12]
and D. Will[1,12]

[1]*Department of Astronomy, The Ohio State University, 140 West 18th Avenue, Columbus, OH 43210, USA*
[2]*Center for Cosmology and Astroparticle Physics, The Ohio State University, 191 W. Woodruff Avenue, Columbus, OH 43210, USA*
[3]*Institute for Astronomy, University of Hawaii, 2680 Woodlawn Drive, Honolulu, HI 96822,USA*
[4]*Carnegie Observatories, 813 Santa Barbara Street, Pasadena, CA 91101, USA*
[5]*Institute for Advanced Study, Princeton, NJ 08540, USA*
[6]*Núcleo de Astronomía de la Facultad de Ingeniería y Ciencias, Universidad Diego Portales, Av. Ejército 441, Santiago, Chile*
[7]*Millennium Institute of Astrophysics, Santiago, Chile*
[8]*Kavli Institute for Astronomy and Astrophysics, Peking University, Yi He Yuan Road 5, Hai Dian District, China*
[9]*Institute of Theoretical Physics, Faculty of Mathematics and Physics, Charles University in Prague, Czech Republic*
[10]*Warsaw University Observatory, Al Ujazdowskie 4, 00-478 Warsaw, Poland*
[11]*The American Association of Variable Star Observers, 49 Bay State Road, Cambridge, MA 02138, USA*
[12]*ASC Technology Services, 433 Mendenhall Laboratory 125 South Oval Mall Columbus, OH 43210, USA*

ABSTRACT

The All-Sky Automated Survey for Supernovae (ASAS-SN) provides long baseline ($\sim$4 yr) light curves for sources brighter than $V \lesssim 17$ mag across the whole sky. As part of our effort to characterize the variability of all the stellar sources visible in ASAS-SN, we have produced $\sim$30.1 million V-band light curves for sources in the Southern hemisphere using the APASS DR9 (AAVSO Photometric All-Sky Survey Data Release) catalogue as our input source list. We have systematically searched these sources for variability using a pipeline based on random forest classifiers. We have identified $\sim$220 000 variables, including $\sim$88 300 new discoveries. In particular, we have discovered $\sim$48 000 red pulsating variables, $\sim$23 000 eclipsing binaries, $\sim$2200 δ-Scuti variables, and $\sim$10 200 rotational variables. The light curves and characteristics of the variables are all available through the ASAS-SN variable stars data base (https://asas-sn.osu.edu/variables). The pre-computed ASAS-SN V-band light curves for all the $\sim$30.1 million sources are available through the ASAS-SN photometry data base (https://asas-sn.osu.edu/photometry). This effort will be extended to provide ASAS-SN light curves for sources in the Northern hemisphere and for $V \lesssim 17$ mag sources across the whole sky that are not included in APASS DR9.

Key words: catalogues – surveys – binaries: eclipsing – stars: variables: δ Scuti.

1 INTRODUCTION

Recent large-scale sky surveys such as the All-Sky Automated Survey (ASAS; Pojmanski 2002), the Optical Gravitational Lensing Experiment (OGLE; Udalski 2003), the Northern Sky Variability Survey (Woźniak et al. 2004), MACHO (Alcock et al. 1997), EROS (Derue et al. 2002), the Catalina Real-Time Transient Survey (CRTS; Drake et al. 2014), the Asteroid Terrestrial-impact Last Alert System (ATLAS; Tonry et al. 2018a; Heinze et al. 2018), and *Gaia* (Gaia Collaboration et al. 2018a,b; Holl et al. 2018) have revolutionized the study of stellar variability. Over time, these surveys have collectively discovered $\gtrsim 10^6$ variable stars across the whole sky.

Variable stars have been used to study astrophysics in multiple contexts. Pulsating variables, including Cepheids, RR Lyrae stars, and Mira variables are used as distance indicators as they follow distinct period–luminosity relationships (PLR, e.g. Leavitt 1908; Matsunaga et al. 2006; Beaton et al. 2018; Whitelock, Feast & Van Leeuwen 2008, and references therein). Eclipsing binary stars

★ E-mail: jayasinghearachchilage.1@osu.edu

are used to study stellar systems and with sufficient radial velocity followup, allow for the derivation of dynamical information and fundamental stellar parameters, including masses and radii of the stars in these systems (Torres, Andersen & Giménez 2010). The precise measurements afforded by studying eclipsing binaries allow for the test of stellar theory across the Hertzsprung–Russell diagram. Variable stars are also used to study stellar populations and Galactic structure (Mateu & Vivas 2018; Matsunaga 2018; Feast & Whitelock 2014).

The All-Sky Automated Survey for SuperNovae (ASAS-SN, Shappee et al. 2014; Kochanek et al. 2017) monitored the visible sky to a depth of $V \lesssim 17$ mag with a cadence of 2–3 d using two units in Chile and Hawaii each with four telescopes. ASAS-SN has recently expanded to 5 units with 20 telescopes. All the current ASAS-SN units are equipped with g-band filters and are currently monitoring the sky to a depth of $g \lesssim 18.5$ mag with a cadence of $\sim$1 d. The ASAS-SN telescopes are hosted by the Las Cumbres Observatory (LCO; Brown et al. 2013) in Hawaii, Chile, Texas, and South Africa. The primary focus of ASAS-SN is the detection of bright supernovae and other transients (e.g. tidal disruption events, cataclysmic variables, AGN flares, stellar flares, etc.) with minimal bias (e.g. Holoien et al. 2014, 2016, 2017, 2018a,b), but its excellent baseline and all-sky coverage allows for the characterization of stellar variability across the whole sky.

In Paper I (Jayasinghe et al. 2018a), we discovered $\sim$66 000 new variables that were flagged during the search for supernovae, most of which are located in regions that were not well sampled by previous surveys. In Paper II (Jayasinghe et al. 2019a), we homogeneously analysed $\sim$412 000 known variables from the International Variable Stars Index (VSX, Watson, Henden & Price 2006), and developed a versatile random forest (RF) variability classifier utilizing the ASAS-SN V-band light curves and data from external catalogues. As data from the Transiting Exoplanet Survey Satellite (TESS; Ricker et al. 2015) became available, we have explored the synergy between the two surveys. The ASAS-SN light curves have long time baselines ($\gtrsim$4 yr) and are sampled at a cadence of $\sim$1–3 d. Thus, these light curves complement the high cadence TESS light curves that have a shorter baseline. In Paper III (Jayasinghe et al. 2019b), we characterized the variability of $\sim$1.3 million sources within $18°$ of the Southern Ecliptic Pole towards the TESS continuous viewing zone and identified $\sim$11 700 variables, including $\sim$7000 new discoveries. We also identified the most extreme heartbeat star system thus known, and characterized the system using both ASAS-SN and TESS light curves (Jayasinghe et al. 2018d). We have also explored the synergy between ASAS-SN and large scale spectroscopic surveys using data from APOGEE (Holtzman et al. 2015) with the discovery of the first likely non-interacting binary composed of a black hole with a field red giant (Thompson et al. 2018) and the identification of 1924 APOGEE stars as periodic variables in Paper IV (Pawlak et al. 2019). During our search for variables, we have also identified numerous unusual, rare variables, including 2 very long period detached eclipsing binaries (Jayasinghe et al. 2018b,c) and 19 R Coronae Borealis stars (Shields et al. 2018).

Here, we extracted the ASAS-SN light curves of $\sim$30.1 million sources from the AAVSO Photometric All-Sky Survey (APASS; Henden et al. 2015) DR9 catalogue with $V < 17$ mag in the Southern hemisphere ($\delta < 0°$). In this work, we systematically search this sample for variable sources. In Section 2, we discuss the input catalogue and the data reduction procedures used to obtain the ASAS-SN light curves. Section 3 discusses the RF-based variability identification and classification procedures. In Section 4, we discuss the ASAS-SN catalogue of variable stars in the Southern hemisphere and present a summary of our work in Section 5.

2 OBSERVATIONS AND DATA REDUCTION

We started with the APASS DR9 catalogue as our input source catalogue. We chose the APASS catalogue because the APASS survey had a faint completeness limit ($V \lesssim 16$) comparable to the ASAS-SN observations. We selected all the APASS sources with $V < 17$ mag in the Southern hemisphere ($\delta < 0°$), excluding the $\sim$1.3M sources towards the Southern Ecliptic Pole which were analysed in Paper III. This resulted in a list of $\sim$30.1M sources. Fig. 1 illustrates the spatial distribution of these sources.

The ASAS-SN V-band observations used in this work were made by the 'Brutus' (Haleakala, Hawaii) and 'Cassius' (CTIO, Chile) quadruple telescopes between 2013 and 2018. Each ASAS-SN V-band field is observed to a depth of $V \lesssim 17$ mag. The field of view of an ASAS-SN camera is 4.5 deg^2, the pixel scale is 8.0 arcsec and the FWHM (full width at half-maximum) is typically $\sim$2 pixels. ASAS-SN tends to saturate at $\sim$10–11 mag, but we attempt to correct the light curves of saturated sources for bleed trails (see Kochanek et al. 2017). The V-band light curves were extracted as described in Jayasinghe et al. (2018a) using image subtraction (Alard & Lupton 1998; Alard 2000) and aperture photometry on the subtracted images with a 2 pixel radius aperture. The APASS catalogue was also used for calibration. We corrected the zero-point offsets between the different cameras as described in Jayasinghe et al. (2018a). The photometric errors were recalculated as described in Jayasinghe et al. (2019b).

While we decided to use the APASS DR9 catalogue as our input source list due to its all-sky coverage, this catalogue has several shortcomings (Henden et al. 2015; Marrese et al. 2019). While the APASS DR9 sky coverage is nearly complete, there are regions towards the Galactic plane that are missing (see Fig. 1). In addition, the DR9 catalogue includes a number of duplicate entries, which appear to be caused by the merging process, where poor astrometry in a given field may cause two centroids to be included for a single source. Centroiding in crowded fields is also poor and blends cause both photometric and astrometric errors. The APASS DR9 catalogue does not provide unique identifiers, thus we used the VizieR (Oelkers et al. 2018) `recno` field as unique identifiers. To address the issue of incomplete sky coverage we will use the ATLAS All-Sky Stellar Reference Catalog (Tonry et al. 2018b) in the next paper to produce light curves for the missing sources in APASS DR9.

3 VARIABILITY ANALYSIS

Here, we describe the procedure we used to identify and characterize variables in the source list. We describe how we cross-matched the APASS sources to external catalogues in Section 3.1. In Section 3.2, we describe the procedure we took to identify candidate variable sources using an RF classifier. In Section 3.3, we discuss the classification of the candidate variables into the various standard classes of variable stars using the V2 RF classifier model from Jayasinghe et al. (2019a), in Section 3.4, we discuss our attempts to mitigate the effects of blending on the list of candidate variables and in Section 3.5, we discuss the quality checks that we used to improve the final variables catalogue.
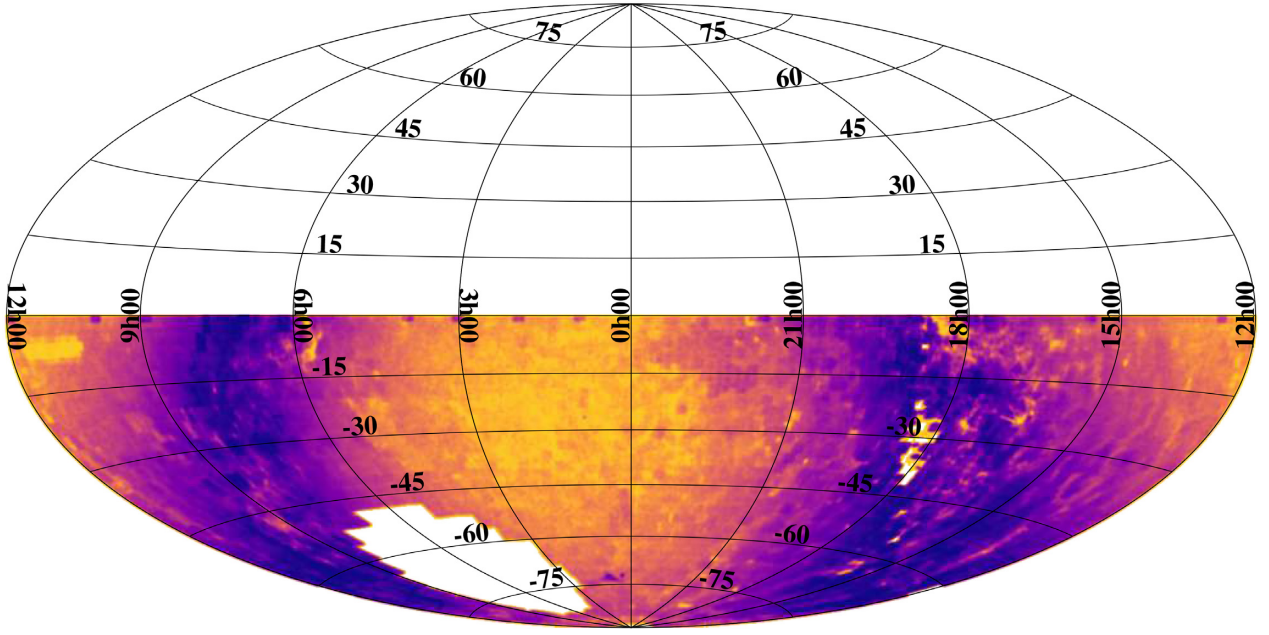
Figure 1. Sky density plot of the ∼30.1M APASS DR9 sources analysed in this work. Sources in the gap centred at the Southern Ecliptic Pole ($\alpha = 6$ h, $\delta = -66.55°$) were analysed in Jayasinghe et al. (2019b). The gaps near ($\alpha = 18$ h, $\delta = -30°$) are in the input APASS DR9 catalogue.

Table 1. Variability features and their importances for variable star identification.

Feature	Description	Importance (per cent)	Reference
LS_Per	Best Lomb–Scargle period	1	–
LS_Pow	Power corresponding to the best Lomb–Scargle period	24	–
log(LS_FAP)	Base 10 logarithm of the FAP corresponding to the best Lomb–Scargle period	11	–
T(t)	Lafler–Kinman string length statistic of the light curve sorted by time	4	Jayasinghe et al. (2019a)
T(ϕ|P)	Lafler–Kinman string length statistic of the light curve sorted by phase	18	Jayasinghe et al. (2019a)
δ	Normalized difference between T(t) and T(ϕ|P)	5	Jayasinghe et al. (2019b)
Skew	Skewness of the magnitude distribution	2	–
Kurt	Kurtosis of the magnitude distribution	2	–
Median	Median of the magnitude distribution	1	–
σ	Standard deviation of the light curve	2	–
IQR	Difference between the 75th and 25th percentiles in magnitude	2	–
A_{HL}	Ratio of magnitudes brighter or fainter than the average	2	Kim & Bailer-Jones (2016)
MAD	Median absolute deviation of the light curve	2	–
$1/\eta$	Inverse of the η (Von Neumann index) value for the light curve	3	Von Neumann et al. (1941)
$J - K_s$	2MASS $J - K_s$ colour	12	Skrutskie et al. (2006)
$H - K_s$	2MASS $H - K_s$ colour	9	Skrutskie et al. (2006)

Table 2. Overall performance of the ASAS-SN RF source classifier.

Class	Precision (%)	Recall (%)	F_1 score (%)	Sources
CONST	99	99	99	600 000
VAR	98	98	98	302 021

3.1 Cross-matches to external catalogues

We cross-match the APASS DR9 sources with *Gaia* DR2 (Gaia Collaboration et al. 2018a) using a matching radius of 5.0 arcsec. The sources were also cross-matched to the *Gaia* DR2 probabilistic distance estimates from Bailer-Jones et al. (2018). Even though we used a liberal matching radius, ∼84 per cent (∼94 per cent) of the sources have a cross-match in *Gaia* DR2 within 2.0 (3.0) arcsec.

These sources were also cross-matched with the Two Micron All Sky Survey (2MASS, Skrutskie et al. 2006) and AllWISE (Cutri et al. 2013; Wright et al. 2010) catalogues using a matching radius of 10.0 arcsec. The cross-matches to these catalogues provide useful information that are later used in the identification and classification of variable stars. We used TOPCAT (Taylor 2005) to cross-match the APASS sources with these external catalogues.

Sources in the Small Magellanic Cloud (SMC) are also included in our input source list. We used association information from *Gaia* DR2 (Gaia Collaboration et al. 2018c) to identify ∼1600 sources from our source list that are SMC members. For sources in the SMC, we use a distance of $d = 62.1$ kpc (Graczyk et al. 2014) in our variability classifier instead of the distance estimate from Bailer-Jones et al. (2018). The LMC was covered in Paper III.
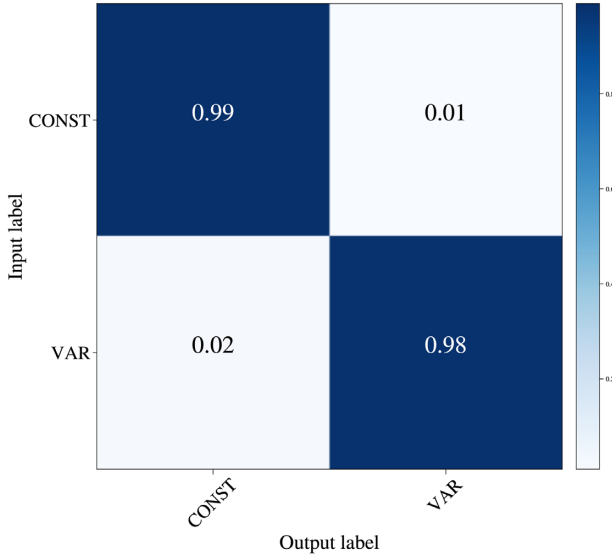
Figure 2. The normalized confusion matrix derived from the final version of the trained RF classifier. The *y*-axis corresponds to the 'input' classification, while the *x*-axis is the 'output' prediction obtained from the trained RF model.

3.2 Random forest variable identification

In Paper III, we used several methods, including linear cuts on Lomb–Scargle periodogram statistics, light-curve features, and external photometry to identify variable sources. Here, we take a different approach by training and apply an RF classifier to distinguish candidate variables from constant sources. We built a variability classifier based on an RF model using scikit-learn (Pedregosa et al. 2012; Breiman 2001). An RF classifier is an ensemble of decision trees whose output is the mean prediction of the individual decision trees (Breiman 2001). The set of variable sources used to train this classifier consisted of ∼302 000 variables from Papers II and III with definite classifications. Variables with uncertain classifications, including 'VAR' and 'ROT:', were not included in this list as they reduced the accuracy of the final RF classification model. The set of constant sources in the training list consisted of ∼600 000 sources randomly selected from the list of constant sources in Paper III.

The goal was to provide classifications into two broad groups: CONST (constant stars) and VAR (potential variables). The potential variables will be analysed in further detail so it is more important not to lose real variables than to accidentally include non-variables. These broad classes were selected to reduce the complexity of the classifier, and to provide an accurate initial separation prior to reclassifying the variable sources with the RF variable type classifier from Paper II. To generate periodicity statistics, we used the ASTROPY implementation of the Generalized Lomb–Scargle (GLS, Zechmeister & Kürster 2009; Scargle 1982) periodogram to search for periodicity over the range $0.05 \leq P \leq 1000$ d in all ∼30.1M light curves. The GLS periodogram is an extension of the standard Lomb–Scargle periodogram that uses a frequency-dependent light-curve mean,

$$y_{\text{model}}(t; f) = y_0(f) + A_{\text{f}} \sin\big(2f(t - \phi_{\text{f}})\big),$$

(equation 41 from VanderPlas 2018). This floating-mean model is more robust if there are gaps in the phased data than the standard Lomb–Scargle periodogram (VanderPlas 2018). We utilize the best

GLS period, false alarm probability (FAP) and the power of the best GLS period as features. The best GLS period is defined to be the period with the largest power which is essentially a measure of the signal-to-noise ratio (S/N) of the periodogram peak. The FAP is the probability that a light curve with no signal would lead to a GLS peak of a similar magnitude (VanderPlas 2018).

We further characterize the periodicity of the light curves using the Lafler–Kinmann string length statistic (Lafler & Kinman 1965; Clarke 2002). We use the definition

$$T(\phi|P) = \frac{\sum_{i=1}^{N}(m_{i+1} - m_i)^2}{\sum_{i=1}^{N}(m_i - \overline{m})^2} \times \frac{(N-1)}{2N} \tag{1}$$

from Clarke (2002), where the m_i are the magnitudes sorted by phase and $\overline{m}$ is the mean magnitude. We also calculate the statistic $T(t)$ after sorting the light curve by time instead of phase. The complete list of 16 features and their importances to the trained RF model is summarized in Table 1. Feature importances are calculated as Gini importances using the mean decrease impurity algorithm (Pedregosa et al. 2012).

The overall results of the RF model are evaluated based on the

$$\text{precision} = \frac{\alpha}{\alpha + \beta}, \tag{2}$$

$$\text{recall} = \frac{\alpha}{\alpha + \gamma}, \tag{3}$$

and the harmonic mean of the two,

$$F_1 = 2 \left(\frac{\text{precision} \times \text{recall}}{\text{precision} + \text{recall}} \right), \tag{4}$$

where α, β, and γ are the number of true positives, false positives, and false negatives in a given class, respectively. These quantities are evaluated for both the constant (CONST) and variable (VAR) sources (Table 2).

The parameters of the RF model were optimized using cross-validation to maximize the overall F_1 score of the classifier. The number of decision trees in the forest was initialized to n_estimators = 1000. We also limited the maximum depth of the decision trees to max_depth = 16 in order to mitigate overfitting, set the number of samples needed to split a node as min_samples_split = 10 and set the number of samples at a leaf node as min_samples_leaf = 5. To further minimize overfitting, we also assigned weights to each class with class_weight = 'balanced_subsample'. For any given source, the RF classifier assigns classification probabilities Prob(Const) and Prob(Var) = 1 − Prob(Const). The output classification of the RF classifier is the class with the highest probability. We split the training sample for training (80 per cent) and testing (20 per cent) in order to evaluate the performance of the RF classifier. The confusion matrix for the trained RF model is shown in Fig. 2. The greatest confusion (2 per cent) arises from input variable sources that are subsequently classified as constant stars. The performance of the classifier is summarized in Table 2. The overall F_1 score for the classifier is 98.5 per cent.

We further investigate the performance variation of the RF classifier with magnitude by binning the test sample by the median *V*-band magnitude (Table 3). The F_1 score for the classifier is lowest (92.9 per cent) for sources with $V \leq 11$ mag where 15 per cent of the input constant sources are incorrectly classified as variable sources. This is likely due to saturation artifacts that arise at these bright magnitudes. The F_1 score varies by < 1 per cent between $11 < V \leq 17$ mag and the confusion between constant and variables sources is

Table 3. Performance of the ASAS-SN RF source classifier with magnitude.

Median magnitude	F_1 score (%)	Constant star false positive rate (%)	Variable star false positive rate (%)	Sources (%)
$V \leq 11$ mag	92.9	15	2	3.1
$11 < V \leq 13$ mag	98.5	1	2	11.5
$13 < V \leq 15$ mag	98.9	1	1	37.5
$15 < V \leq 17$ mag	98.4	1	3	47.3
$V \geq 17$ mag	95.5	5	4	0.8
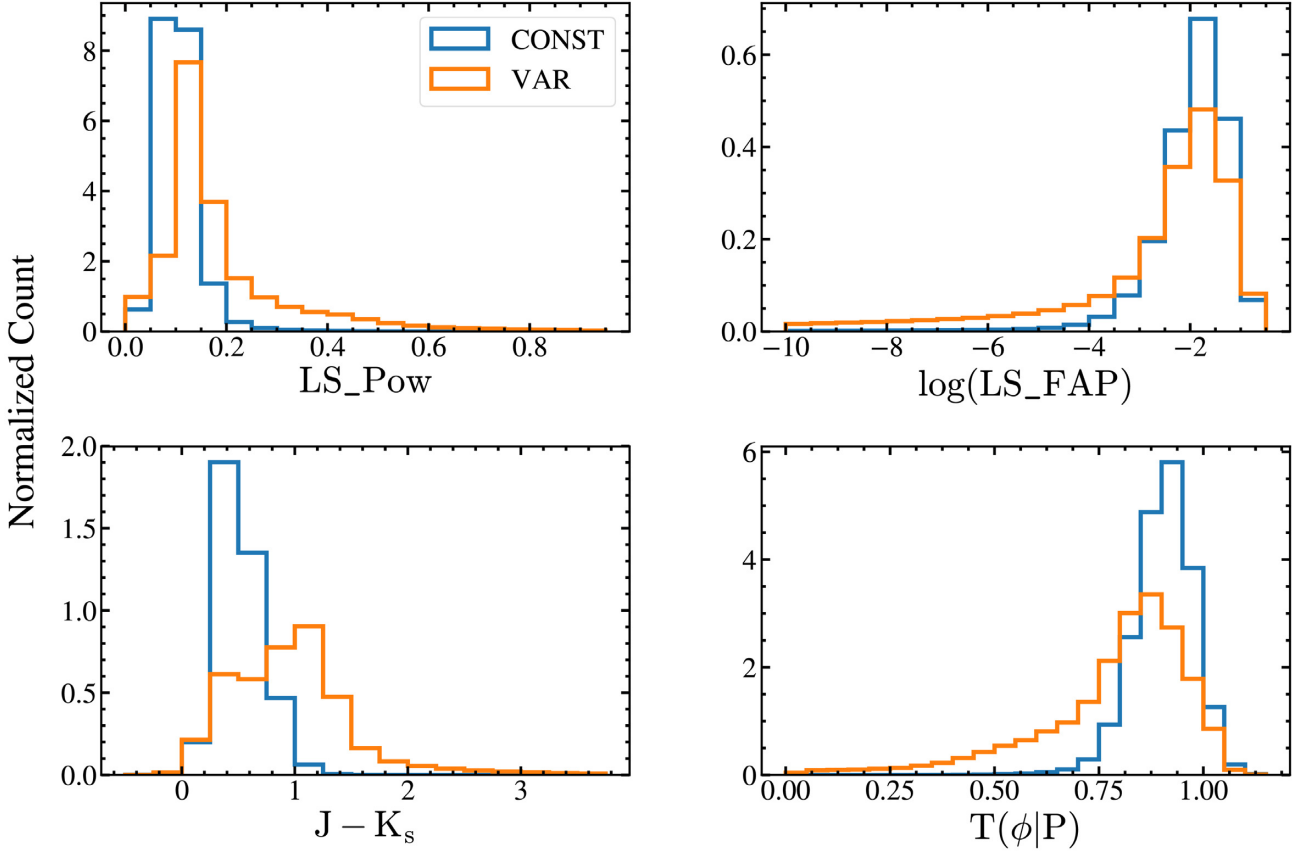
Figure 3. Distribution of the sources classified as CONST and VAR in the LS_Pow, T(ϕ|P), $J - K_s$, and log(LS_FAP) features. Sources with log(LS_FAP)< -10 are not shown for clarity.

also minimal. Most of the sources (96.3 per cent) in the test sample have median magnitudes that fall within this range. For sources at the ASAS-SN *V*-band faint limit of $V \geq 17$ mag, the F_1 score drops to 95.5 per cent and the confusion between classes again rises. This is not surprising as at these magnitudes the light curves are dominated by noise.

We applied the trained RF classifier to the entire sample of ~30.1M sources and identified 3 553 235 candidate variables. The distinction between the constant sources and the candidate variables is illustrated in Fig. 3 through the distributions of the four features with the largest importance: LS_Pow, T(ϕ|P), $J - K_s$ and log(LS_FAP). We find that many candidate variable sources are strongly periodic with high values of LS_Pow and smaller values of log(LS_FAP) and T(ϕ|P). In addition, the distribution of the 2MASS colour $J - K_s$ differs significantly between constant and variable sources. Variable sources are skewed towards redder near-infrared (NIR) colours with $J - K_s > 1$ mag while constant sources largely peak around $J - K_s \sim 0.5$ mag. Cooler, evolved stars are more likely to be variable, so this is not unexpected. Nevertheless, the

distributions of constant and variable sources overlap significantly in the feature spaces illustrated in Fig. 3. It is crucial to note that while we illustrated these distributions linearly, the RF classifier is inherently non-linear and relies on a complex ensemble of decision trees to predict the class of any given source. In this sense, even the features with the least importance do matter for the overall success of the classifications.

3.3 Variability classification

Once candidate variables are identified, we aimed at classifying these sources into the various standard classes of variable stars. We use the variability classifier implemented in Jayasinghe et al. (2019a), which consists of an RF classifier plus several refinement steps. Given the large number of candidates, we changed our variability classification strategy as follows.

(i) Initially, we classified all the candidate variables using just the GLS periods derived in *Section* 3.2.

Table 4. Summary of the variability refinement criteria for each variable class.

Class	Summarized refinement criteria
δ Scuti (HADS, DSCT)	Skew < 0.15, LS_Pow>0.25, log(LS_FAP)<−7, A < 0.5 mag, T(ϕ|P) < 0.5, −1 < W_{JK} < 3 mag
RR Lyrae (RRAB, RRC, RRD)	RRAB and log(LS_FAP)<−10, LS_Pow>0.2, A > 0.08 mag, T(ϕ|P) < 0.6, Skew < 0.15, δ < −0.25
	RRC/RRD and log(LS_FAP)<−10, LS_Pow>0.2, A > 0.08 mag, T(ϕ|P) < 0.6, Skew < 0, δ < −0.25
Cepheids (DCEP, DCEPS, CWA, CWB, RVA)	Skew < 1, log(LS_FAP)<−10, LS_Pow>0.3, A < 2 mag, T(ϕ|P) < 0.6, δ < −0.25
Rotational variables (ROT	Period>0.6 d and log(LS_FAP)<−5, LS_Pow>0.2, A > 0.08 mag, T(ϕ|P) < 0.6, δ < 0
	Period≤0.6 d and W_{JK} > 2.5 mag, Prob > 0.9
Eclipsing binaries (EA, EB, EW)	EA (GLS) and α < 100, T(ϕ|P) < 0.6, A > 0.08 mag
	EB (GLS) and log(LS_FAP)<−7, LS_Pow>0.2, A > 0.08 mag, T(ϕ|P) < 0.6
	EW (GLS) and log(LS_FAP)<−7, LS_Pow>0.2, A > 0.08 mag, T(ϕ|P) < 0.6, Skew > 0
	EA (BLS) and α < 100, T(ϕ|P) < 0.45, Prob > 0.8
Semiregular and irregular variables (SR, L)	α < 5, V_{mean} > 11 mag, A > 0.08 mag
	Period>100 d and log(LS_FAP)<−3, $J − K_s$ > 1.1, A > 0.1 mag, T(t) < 0.7
	10 ≤Period≤100 d and log(LS_FAP)<−8, A > 0.08 mag
Mira variables (M, M:)	log(LS_FAP)<−3, LS_Pow>0.5 , T(ϕ|P) < 0.5
YSO	Period<100 d and α < 5, log(LS_FAP)<−10, LS_Pow>0.25, T(ϕ|P) < 0.6
Outbursting Be stars (GCAS, GCAS:)	α < 5, V_{mean} > 11 mag, $J − K_s$ < 1.1, 0.25 < A < 1 mag, T(t) < 0.5
Generic variables (VAR)	α < 5, 0.1 < A < 2 mag, W_{JK} > −4 mag, V_{mean} > 11 mag, T(ϕ|P) < 0.5 OR T(t) < 0.5

Table 5. Variables by type.

VSX Type	Description	Known	New
CWA	W Virginis type variables with P > 8 d	205	51
CWB	W Virginis type variables with P < 8 d	225	45
DCEP	Fundamental mode Classical Cepheids	645	16
DCEPS	First overtone Cepheids	171	9
DSCT	δ Scuti variables	744	1354
EA	Detached Algol-type binaries	11413	9948
EB	β Lyrae-type binaries	8574	4115
EW	W Ursae Majoris type binaries	27926	8887
HADS	High-amplitude δ Scuti variables	1338	849
M	Mira variables	3472	38
ROT	Rotational variables	7200	10236
RRAB	RR Lyrae variables (Type ab)	12936	294
RRC	First overtone RR Lyrae variables	2655	1015
RRD	Double-mode RR Lyrae variables	233	12
RVA	RV Tauri variables (Subtype A)	32	0
SR	Semiregular variables	44198	45556
L	Irregular variables	4979	2528
GCAS	γ Cassiopeiae variables	20	8
YSO	Young stellar objects	1949	980
GCAS:	Uncertain γ Cassiopeiae variables	20	6
VAR	Generic variables	2789	2343

(ii) Following this, we derive periods for a limited set of sources (see below) using the `astrobase` implementation (Bhatti et al. 2018) of the Box Least Squares (BLS, Kovács, Zucker & Mazeh 2002) periodogram to improve the completeness for eclipsing binaries whose periodicity cannot be easily identified with GLS.

We also run the variability classifier twice, once using the best period (GLS or BLS) and once using twice the best period. The final classification is the one which yields the greatest classification probability. This step greatly improves the separation of EW type

eclipsing binaries from RRC variables, and also improves upon the efficiency of the automated period doubling algorithm that was used for eclipsing binaries in Paper II.

To identify possible eclipsing binaries, we selected ∼576 000 candidate variables with A_{HL} > 2 (Table 1) from our original list. A_{HL} is the ratio of magnitudes brighter or fainter than the average magnitude (Kim & Bailer-Jones 2016). Since eclipses usually only span limited phase ranges, A_{HL} tends to be higher for the light curves of eclipsing binaries compared to other variable types. We searched for periods over the range 0.05 ≤ P ≤ 1000 d and the BLS
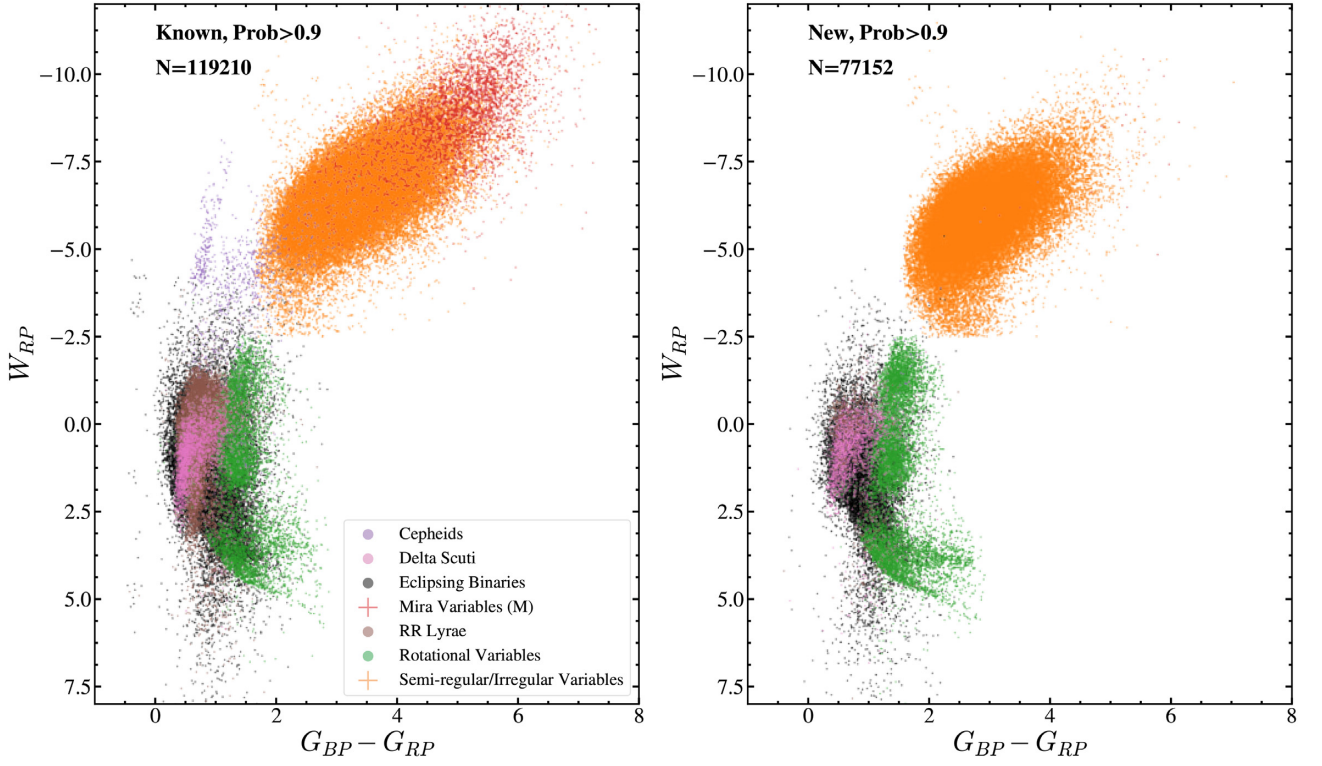
Figure 4. The Wesenheit W_{RP} versus $G_{BP} - G_{RP}$ CMD for the variables with Prob > 0.9, that have already been discovered (left), and the new discoveries (right).

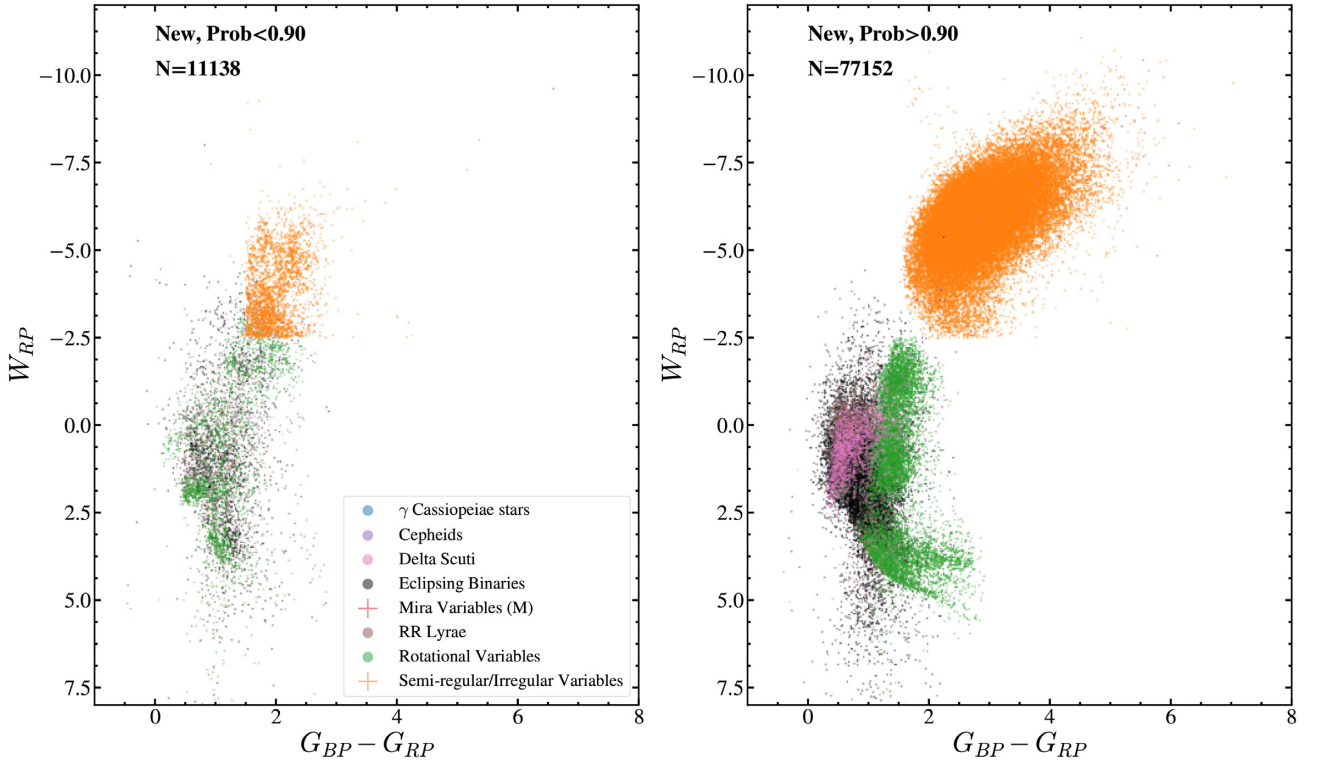**Figure 5.** The Wesenheit W_{RP} versus $G_{BP} - G_{RP}$ CMD for the newly discovered variables with Prob < 0.9 (left), and Prob > 0.9 (right).
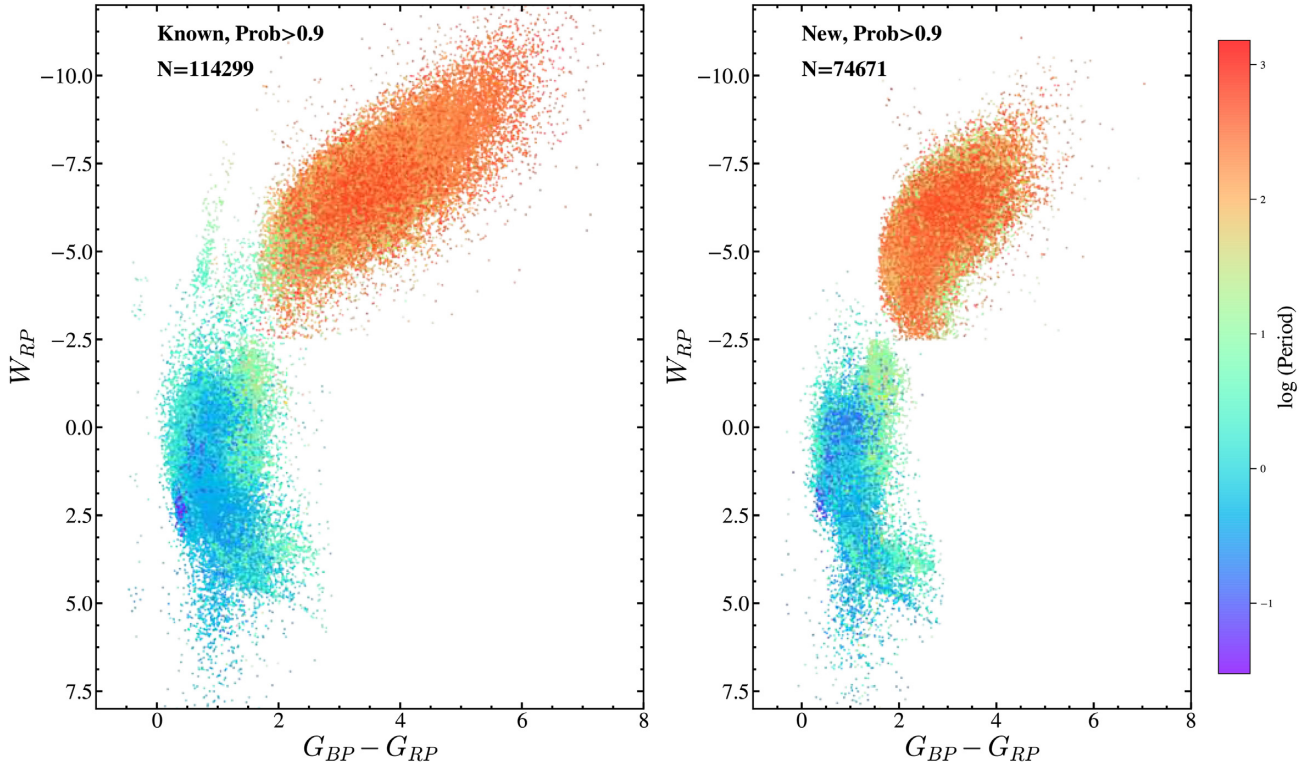
Figure 6. The Wesenheit W_{RP} versus $G_{BP} - G_{RP}$ CMD for the periodic variables with Prob > 0.9, that have already been discovered (left), and the new discoveries (right). The points are coloured by the period.
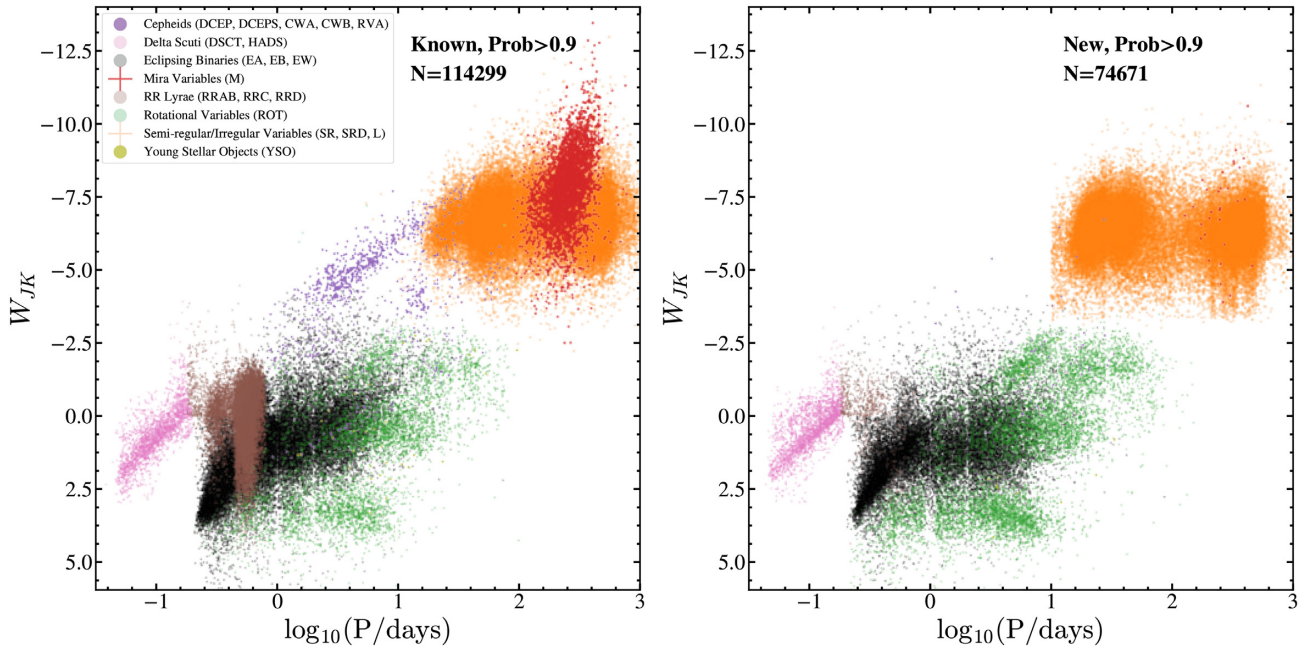
Figure 7. The Wesenheit W_{JK} PLR diagram for the periodic variables with Prob > 0.9, that have already been discovered (left), and the new discoveries (right).

periodogram was initialized with 200 phase bins and a minimum (maximum) transit duration of 0.1 (0.3) in phase. BLS periods were only selected if the BLS power was <0.3. We identified ~3500 eclipsing binaries through this process.

3.4 Blending corrections

Blending towards crowded regions (e.g. the Galactic disc) is problematic owing to the large pixel scale (8.0 arcsec) and the FWHM (~16.0 arcsec) of the ASAS-SN images. The APASS data
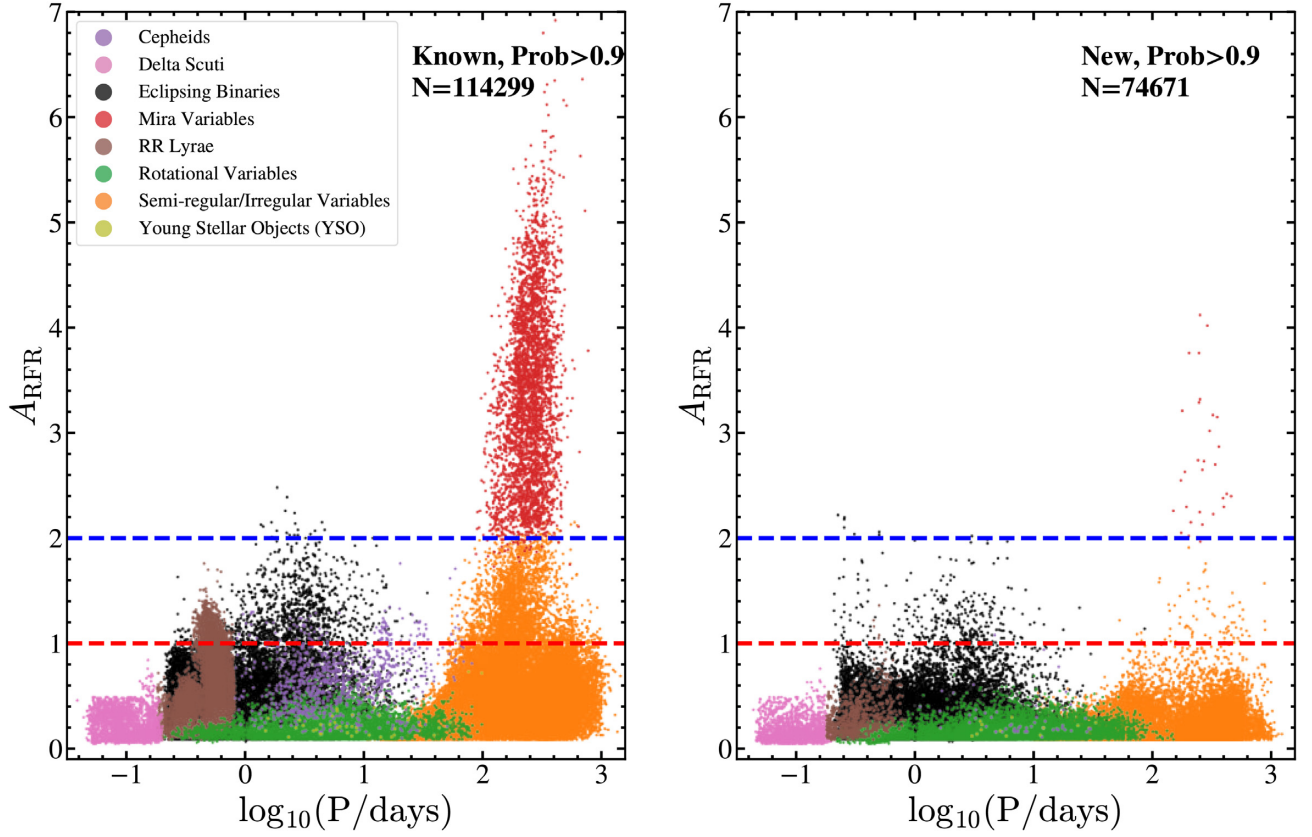
Figure 8. Period–amplitude plot for the for the periodic variables with Prob > 0.9, that have already been discovered (left), and the new discoveries (right). Reference amplitudes of 1 and 2 mag are shown in red and blue, respectively.
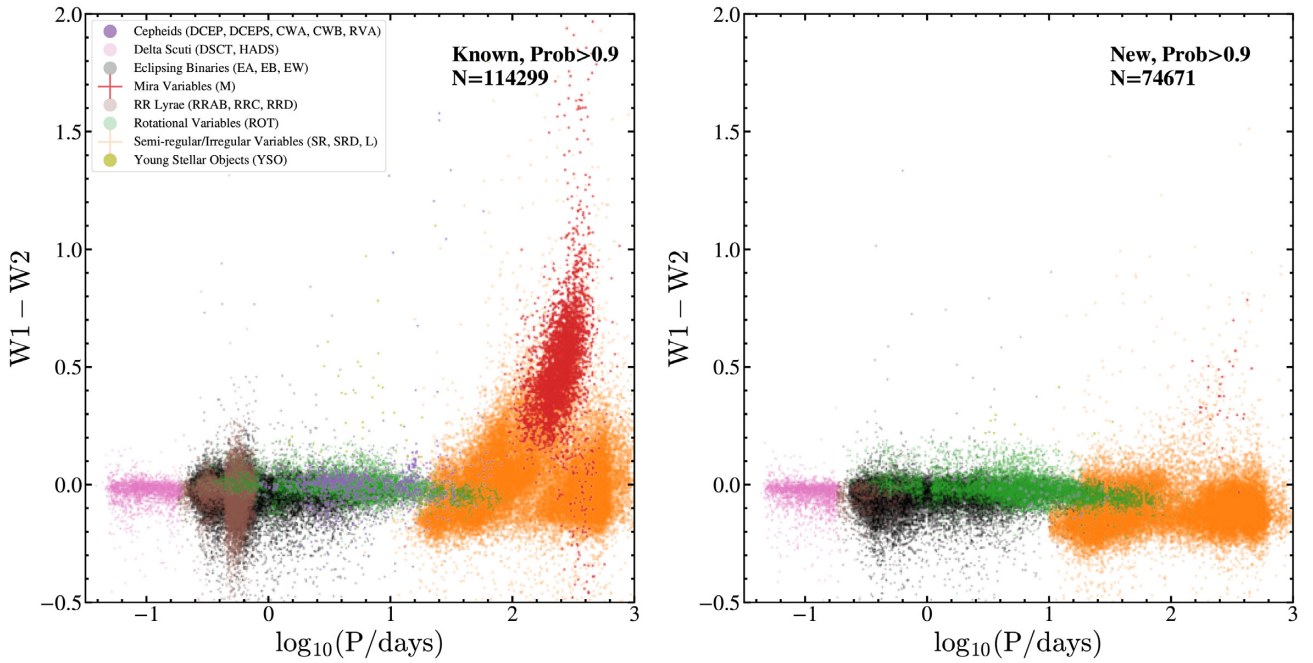
Figure 9. The period versus $W_1 - W_2$ colour diagram for the variables with Prob > 0.9, that have already been discovered (left), and the new discoveries (right).
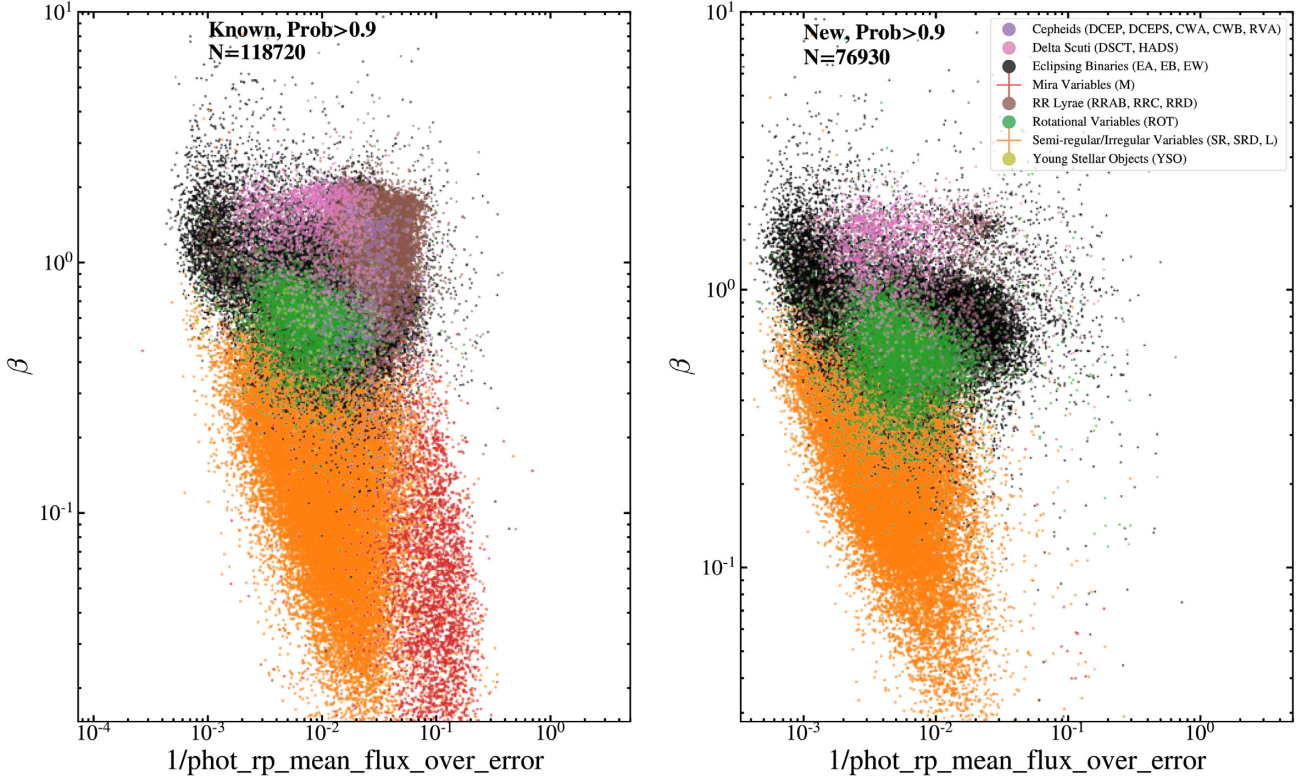
Figure 10. The *Gaia* DR2 BP/RP variability ratio β against 1/phot_rp_mean_flux_over_error.

have a significantly smaller pixel scale (2.6 arcsec), so we can have multiple APASS sources inside a single ASAS-SN resolution element. To minimize the number of false positives in our catalogue of variables due to blending, we identify and correct blended variable groups in our catalogue. However, we have not attempted to correct for the contaminating light in the photometry of the blended sources.

We find that ∼1.1M of the ∼3.6M candidate variables had at least one neighbour within 30.0 arcsec from their positions. For these sources, we compute the flux variability amplitudes using a non-parametric RF regression model (Jayasinghe et al. 2019a). We then identify groups of blended variables based on the cross-matching. For each blended variable group, we select the source with the largest flux variability as the 'true' variable, and discard the remaining overlapping sources in the blended group from the final list. After removing these overlapping, blended sources from the list of candidate variables, we were left with ∼3M sources.

3.5 Quality checks

At this stage, visual review of a random set of light curves suggested that quality checks must be implemented to distinguish *true* variability signals from variability due to bad photometry, and other survey specific issues (e.g. shutter failures, etc.). In Paper III, given the significantly shorter list of candidate variables, this was accomplished through simple visual review of the light curves. In this work, given the shear number of sources, visual review is not a feasible option. Thus, we choose to implement various criteria in lieu of visual review, to distinguish the true variables from the 'noise'.

We first restrict the list to sources with $V_{\mathrm{mean}} > 10$ mag, $A > 0.05$ mag, and $T(t) < 0.9$. We implemented the cut in the ASAS-SN

V-band magnitude to minimize noise due to saturation artefacts. We also calculate the ratio between the amplitude estimated by RF regression (A) to the interquartile range IQR (Table 1) of the light curve,

$$\alpha = A/\mathrm{IQR}, \tag{5}$$

and the absolute, reddening-free Wesenheit magnitudes (Madore 1982; Lebzelter et al. 2018)

$$W_{\mathrm{RP}} = M_{G_{\mathrm{RP}}} - 1.3(G_{\mathrm{BP}} - G_{\mathrm{RP}}), \tag{6}$$

and

$$W_{\mathrm{JK}} = M_{K_{\mathrm{s}}} - 0.686(J - K_{\mathrm{s}}), \tag{7}$$

for each source, where the G_{BP} and G_{RP} magnitudes are from *Gaia* DR2 (Gaia Collaboration et al. 2018a) and the J and K_{s} magnitudes are from 2MASS (Skrutskie et al. 2006). The Wesenheit magnitudes are used in the pipeline from Paper II to refine variable type classifications. The quantity α can be used to identify light curves with significant outliers as we expect $\alpha \approx 2$ for most sources.

The criteria used in lieu of visual review are summarized in Table 4. We note that these criteria are applied in addition to the refinement criteria in Paper II. These are not replacements but additional quality checks intended to improve the purity of our catalogue. We derived these criteria through visual inspection in order to minimize false positives in the different variable groups. In addition to the criteria summarized in Table 4, we further scrutinize sources with periods that are close to aliases of a sidereal day (e.g. $P \approx 1, 2, 30$ d, etc.). This is accomplished by tightening the criteria on T(ϕ|P), log(LS_FAP), LS_Pow, and δ. This process slightly reduces the completeness of our catalogue at these periods, but greatly reduces the number of false positives. In addition, we removed QSO contaminants in this list by cross-matching our list of
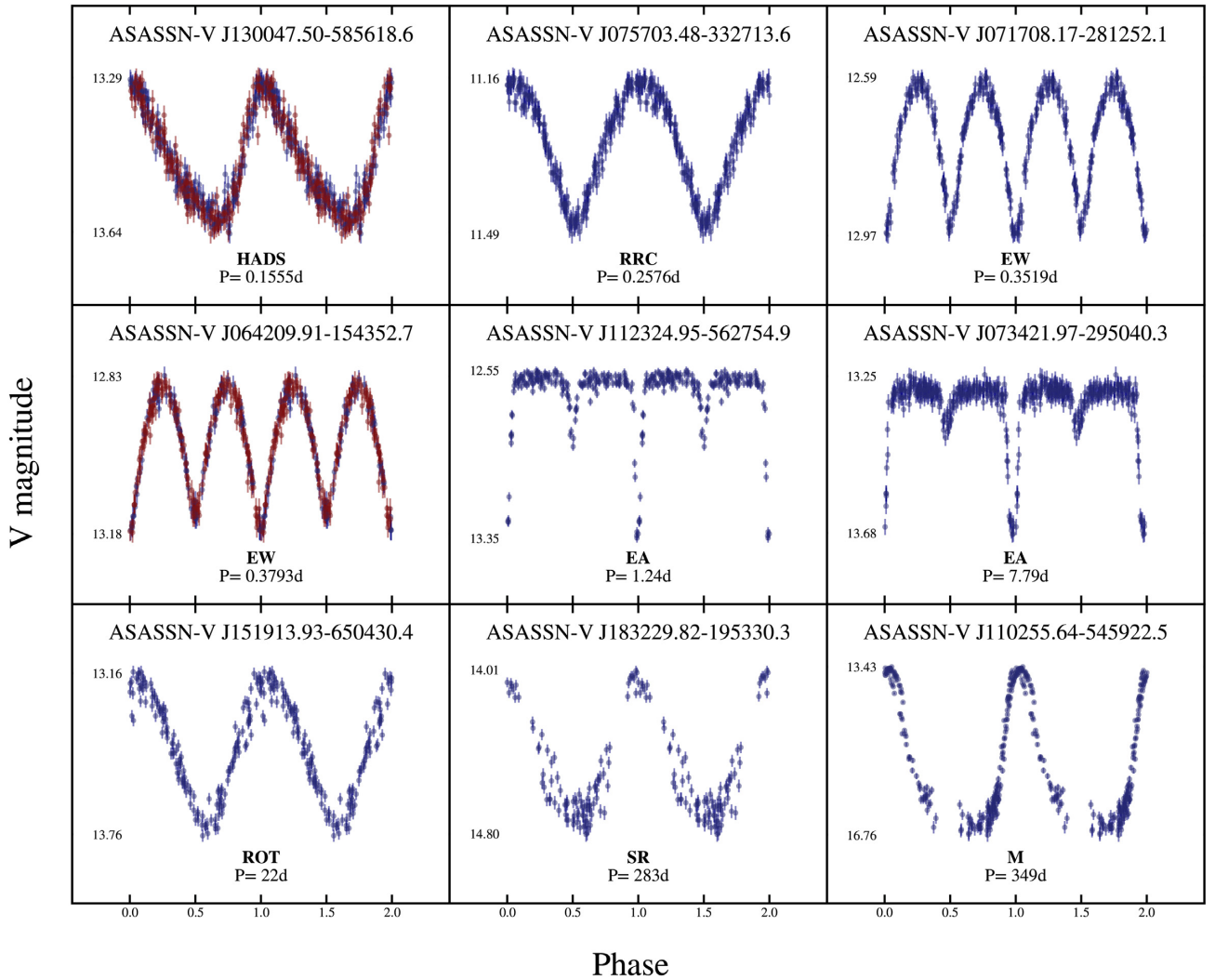
Figure 11. Phased light curves for examples of the newly discovered periodic variables. The light curves are scaled by their minimum and maximum *V*-band magnitudes. Different coloured points correspond to data from the different ASAS-SN cameras. The different variability types are defined in Table 5.

variables to the Liao et al. (2019) catalogue of known QSOs using a matching radius of 5.0 arcsec. We identified 336 cross-matches, out of which 325 were classified as young stellar objects (YSO) variables in our pipeline. At this point, we had ~247 200 sources nominally classified as variable stars.

We inspected 5000 randomly selected sources classified as non-variable and the same number classified as variable. This was partly just a sanity check but also driven by the concern that the large size of our initial list (~10 per cent of the sources) suggested that our false positive rates had to be higher than suggested by Table 2. Among the non-variable sources, we identified only 3 (~ 0.06 per cent) that might be low level variables, which suggests that we are missing few variables that can be detected in this data. For the variable stars, we found significant numbers of false positives in the following variable classes: GCAS (~50 per cent), L (~25 per cent), VAR (~45 per cent), and YSO (~13 per cent). The implied false positive rate for the variable sources was ~5.9 per cent at this point.

Light curves that are contaminated by systematics tend to be classified as irregular or generic variables as they are inherently aperiodic in nature. Thus, we decided to review all ~32 800 sources

that were classified as L, VAR, GCAS, or YSO to improve the purity of our catalogue. Initial results suggested that L variables with $T(t) >$ 0.65 were dominated by noise, so we rejected ~14 300 such sources without further visual review. We visually reviewed the remaining ~18 500 sources, and rejected ~12 600 sources (~68 per cent) and only retained ~5900 of these sources in the final catalogue. When we carried out a new inspection of 5000 randomly selected variables, the false positive rates were now EA (~1.4 per cent), L (~0.6 per cent), SR (~2.6 per cent), and VAR (~0.9 per cent). This implies an overall false positive rate for the final catalogue of variable sources of ~ 1.3 per cent.

After these criteria are applied, we end up with a list of ~220 000 variables. This means that our initial candidate list had a false positive rate of ~93 per cent. The larger than expected false positive rate is partly due to a biased training set in the source classifier. The training set of constant sources was derived from a region of the sky away from the Galactic plane. The increased crowding and blending towards the Galactic plane will systematically affect constant stars at low latitudes and introduce spurious variability signals into their light curves. Our classifier will identify these constant sources as candidate variables. In addition to this, sources
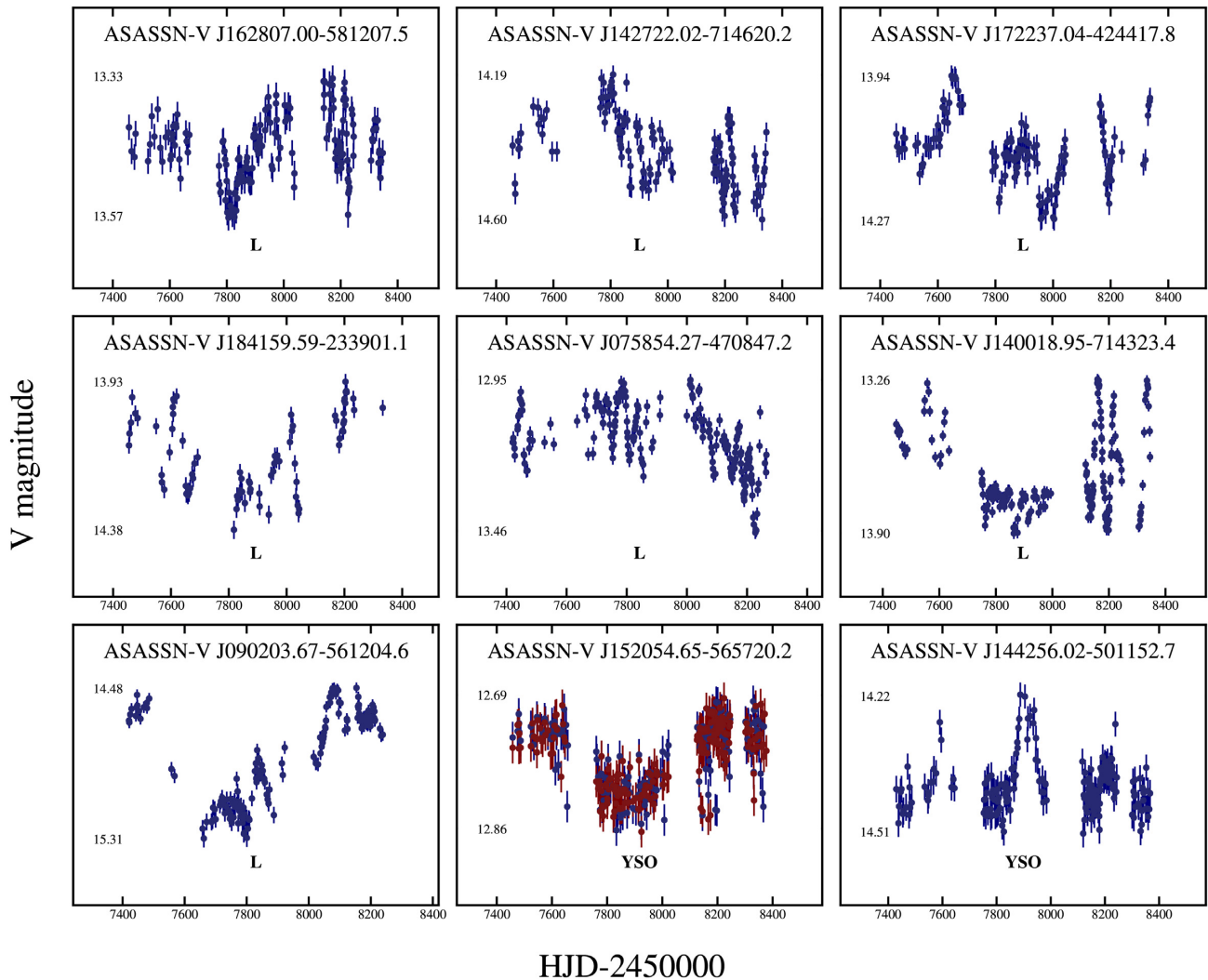
Figure 12. Light curves for examples of the newly discovered irregular variables. The format is the same as for Fig. 11.

in the vicinity of bright, saturated stars in our data are likely to have spurious variability signals in their image subtraction light curves due to the corrections made for bleed trails (see Kochanek et al. 2017). This effect is again exacerbated towards the Galactic plane.

4 RESULTS

The complete catalogue of ∼220 000 variables and their light curves are available at the ASAS-SN Variable Stars Database (https://asas-sn.osu.edu/variables) along with the *V*-band light curves for each source. Most of the known variables identified in this work were already added to the variable stars data base in Paper II. We have overhauled the web interface for the ASAS-SN Variable Stars Database to include interactive light-curve plotting and photometry from *Gaia* DR2, APASS DR9, 2MASS, and ALLWISE. Table 5 lists the number of sources of each variability type in the catalogue.

In order to identify known variable stars, we matched our list of variables to the VSX (Watson et al. 2006) catalogue, with a matching radius of 16.0 arcsec. The variables discovered by the ASAS (Pojmanski 2002) and the CRTS (Drake et al. 2014) have already been incorporated into the VSX data base. Numerous other

studies (e.g. Mateu et al. 2012; Fernández-Trincado et al. 2015, and references therein) have also searched for variable stars on a smaller scale (e.g. globular clusters). While some of these results have been included in the VSX catalogue, we note that the inclusion of these studies in the VSX catalogue is likely to be incomplete. We also match our variables to the catalogue of variable stars discovered by ASAS-SN (Jayasinghe et al. 2018a), the catalogues of variable stars in the Magellanic clouds and the Galactic bulge from the OGLE (Udalski 2003; Pawlak et al. 2016; Soszyński et al. 2016; Udalski et al. 2018, and references therein), the catalogue of variables from the ATLAS (Tonry et al. 2018a; Heinze et al. 2018), the *Gaia* DR2 catalogue of variables (Gaia Collaboration et al. 2018a,b; Holl et al. 2018), the catalogue of variables identified by KELT (Oelkers et al. 2018), the catalogue of WISE variables (Chen et al. 2018), and the variables from MACHO (Alcock et al. 1997). Of the ∼220 000 variables identified in this work, ∼131 900 were previously discovered by other surveys, and ∼88 300 are new discoveries, as also listed in Table 5.

It is evident that previous surveys, including our discoveries from Paper I, successfully discovered sources that have large amplitudes or are strongly periodic. Most (∼54 per cent) of our new discoveries are red, pulsating variables. We also discover a large number of binaries and rotational variables, amounting to ∼26 per cent and
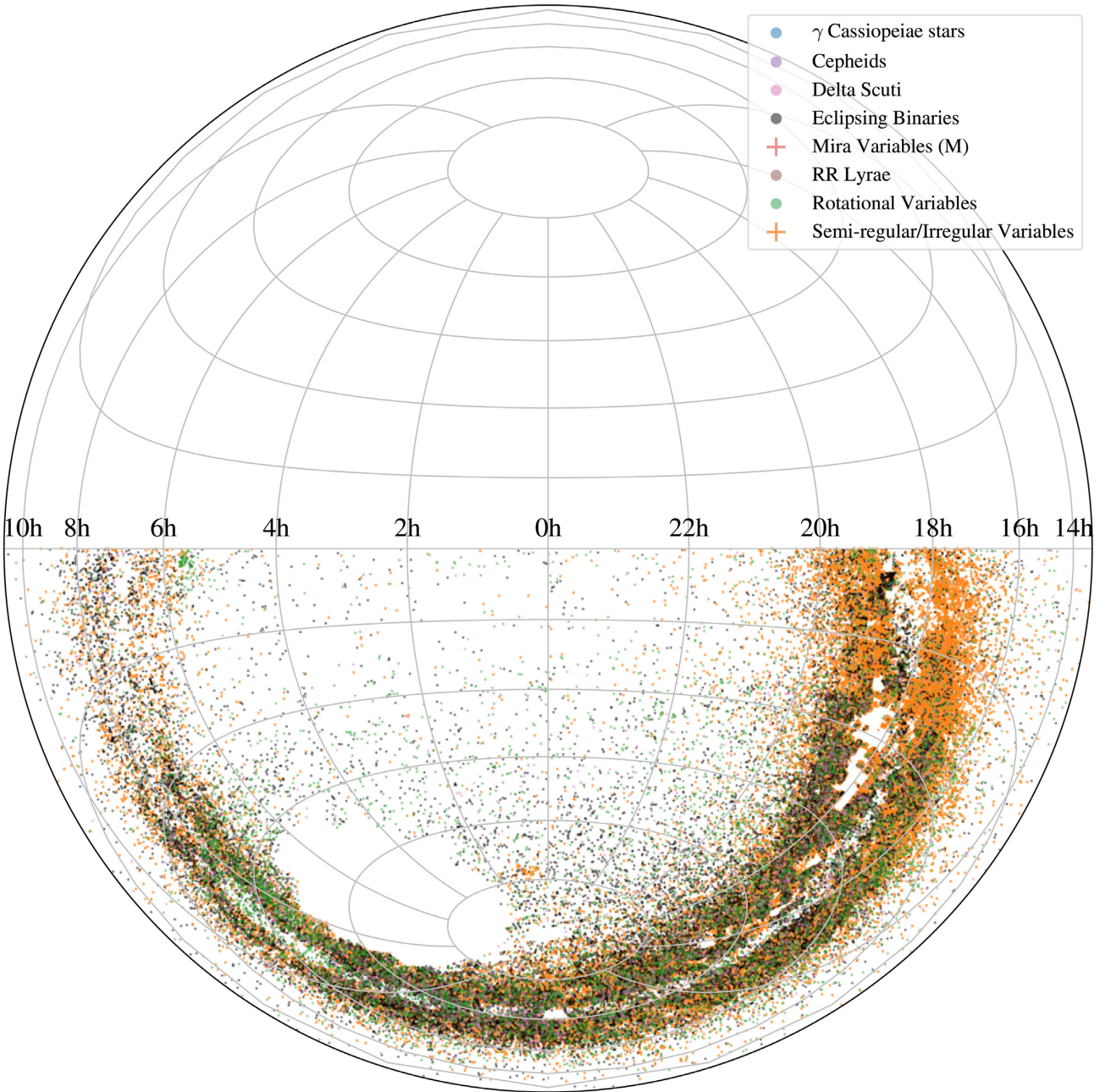
Figure 13. Spatial distribution of the $\sim 88\,300$ newly discovered variables in equatorial coordinates. Sources in the gap centred at the Southern Ecliptic Pole ($\alpha = 6$ h, $\delta = -66.55°$) were analysed in Jayasinghe et al. (2019b). The other gaps are in the APASS catalogue.

~ 12 per cent of the newly discovered variable sources, respectively. It is also noteworthy that we discover many more δ Scuti sources than previously known. These variables are particularly interesting as they pulsate at high frequencies ($P < 0.3$ d) and are located towards the lower end of the instability strip (Breger 1979). δ Scuti variables are also known to follow a PLR (Lopez de Coca et al. 1990).

The Wesenheit W_{RP} versus $G_{BP} - G_{RP}$ colour–magnitude diagram (CMD) for all the variables with excellent variable type classification probabilities (Prob > 0.9) is shown in Fig. 4. Generic and uncertain variable types are not shown. We have sorted the variables into groups to highlight the different classes of variable sources. A similar Wesenheit W_{RP} versus $G_{BP} - G_{RP}$ CMD for all

the newly discovered variables, separated by probability, is shown in Fig. 5. The sharp cut-offs seen in the sample of semiregular variables with Prob < 0.9 are inherited from the variable type refinements from Paper II. Most variables with Prob < 0.9 are located in similar areas of the CMD as the variables with Prob > 0.9. However, we note two interesting clusters of these low-probability variables at $(G_{BP} - G_{RP}, W_{RP}) \sim (2.5, -4.5)$ and $(0.75, 1.8)$ corresponding to semiregular and rotational variables respectively. We plan to further investigate these clusters after the variable sources in the Northern hemisphere have been incorporated into our catalogue.

The Wesenheit W_{RP} versus $G_{BP} - G_{RP}$ CMD for all the variables with Prob > 0.9 and the points coloured according to the period is shown in Fig. 6. This essentially highlights the large dynamic range

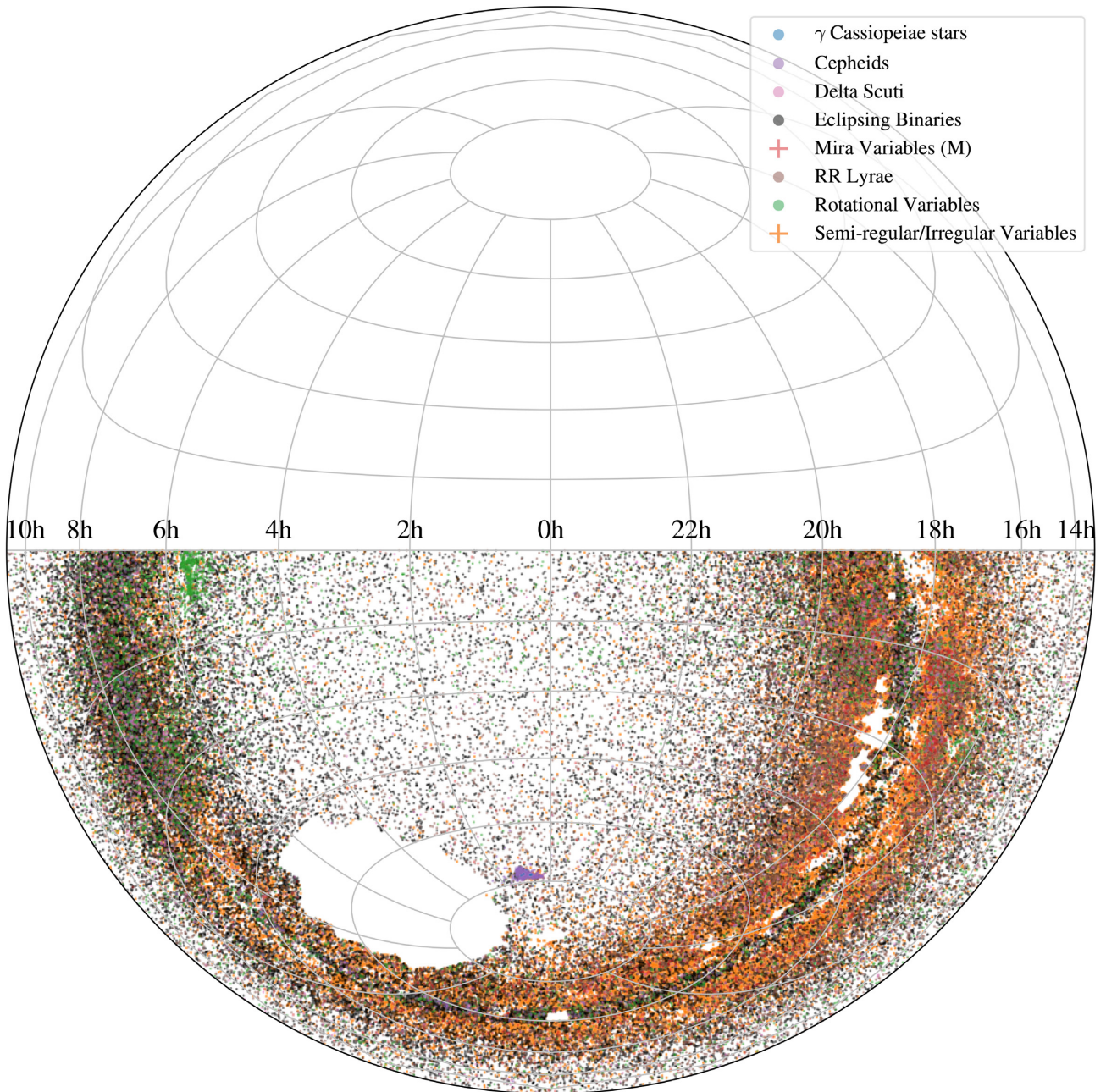**Figure 14.** Spatial distribution of the ∼ 131 900 known variables in equatorial coordinates. Sources in the gap centred at the Southern Ecliptic Pole ($\alpha = 6$ h, $\delta = -66.55°$) were analysed in Jayasinghe et al. (2019b). The other gaps are in the APASS catalogue.

in period probed by the ASAS-SN light curves. Owing to the ASAS-SN survey cadence and our long time baseline, we are able to probe both short-period variability ($P < 0.1$ d) and long-period variability ($P > 1000$ d). The ASAS-SN survey continues to monitor the sky in the g-band, which lends itself well to the analysis of long-term trends and unusual variability. As a testament to this, Jayasinghe et al. (2019c) noted a sudden dimming episode (flux reduction of ∼70 per cent in the g band) in an APASS source (ASASSN-V J213939.3 − 702817.4) that was non-variable for ∼1800 d. This source was classified as a constant source in this work.

The combined Wesenheit W_{JK} PLR diagram for the periodic variables with Prob > 0.9 is shown in Fig. 7. The PLR sequences for the Cepheids are well defined (Soszynski et al. 2005). Sharp PLR

sequences can also be seen for Delta Scuti variables and contact binaries. The Mira variables also form a distinct PLR sequence beyond $P > 100$ d. The slight deficits of variables at the aliases of a sidereal day (e.g. $P \approx 1, 2, 30$ d, etc.) are due to the quality checks implemented in Section 3.5.

The period–amplitude plot for the periodic variables with Prob > 0.9 is shown in Fig. 8. The high prior completeness of the Mira, RR Lyrae, and Cepheid variables is evident. We do not discover many of these variables in this work. The large majority (∼98.7 per cent) of the new discoveries are of different variable types with smaller variability amplitudes and/or weak periodicity.

We also examine the period–colour relationship of the variables in the ALLWISE (Cutri et al. 2013; Wright et al. 2010) $W_1 - W_2$

colour space in Fig. 9. Most variables have $W_1 - W_2 \sim 0$, but the NIR excess increases with increasing period for the long-period variables. This is even more dramatic for the Mira variables. Dust formation is commonly traced through IR excesses. Our findings agree with McDonald et al. (2018), for example, that strong mass loss and increased dust formation first occurs for pulsation periods of $P \gtrsim 60$ d for Galactic stars.

As an external check of our classifications, we used data from our cross-match to *Gaia* DR2 (Gaia Collaboration et al. 2018a) to produce Fig. 10. We define a 'variability' colour β,

$$\beta = \text{phot\_bp\_mean\_flux\_error}/\text{phot\_rp\_mean\_flux\_error} , \quad (8)$$

which is a measure of the difference in variability between the bluer and redder *Gaia* bands and compare it to the inverse of the quantity 'phot_rp_mean_flux_over_error' which is a measure of the mean S/N. The different groups of variables fall in distinct regions, with red pulsating variables having smaller values of β compared to bluer variables. Comparing the known variables and the new discoveries, we find that the new discoveries mostly fall in the same regions as the known variables. This provides an independent confirmation of the purity of the newly discovered variables and validates our quality assurance methodology in Section 3.5.

Examples of the newly identified periodic variables are shown in Fig. 11 and examples of the newly discovered irregular variables are shown in Fig. 12. The light curves for the red giant pulsators, including the irregular variables, are complex, and often multiperiodic, which requires further Fourier analysis. In order to better understand these pulsating red giants, Percy & Fenaux (2019) recommended a more detailed analysis, combining visual inspection of the light curves and a more advanced period analysis, in lieu of the automated classification used by ASAS-SN.

We illustrate the sky distribution of the newly discovered variables in Fig. 13. Most of these discoveries are clustered towards the Galactic disc, as is expected. We note the scarcity of high-amplitude Mira variables, RR Lyrae, and Cepheid variables and the abundance of lower amplitude semiregular/irregular variables among the newly discovered variables. Variables with large amplitudes and strong periodicity are relatively easily discovered and characterized by wide-field photometric surveys, so the existing completeness of these variable types is very high. The gaps in coverage will be rectified in the next paper in this series. We also show the sky distribution of the known variables identified in this work in Fig. 14. Here, we note the abundance of Mira variables, eclipsing binaries, and Cepheid variables that have been discovered by previous surveys.

5 CONCLUSIONS

We systematically searched for variable sources with $V < 17$ mag in the Southern hemisphere ($\delta < 0$ deg), excluding the ~ 1.3M sources near the Southern Ecliptic Pole which were analysed in Paper III. Through our search, we identified $\sim 220\,000$ variable sources, of which $\sim 88\,300$ are new discoveries. The sample of new variables includes $\sim 48\,000$ red pulsating variables, $\sim 23\,000$ eclipsing binaries, ~ 2200 δ-Scuti variables, and $\sim 10\,200$ rotational variables.

The *V*-band light curves of all the ~ 30.1M sources studied in this work are available online at the ASAS-SN Photometry Database (https://asas-sn.osu.edu/photometry). We have also updated the ASAS-SN variable stars data base (https://asas-sn.osu.edu/variables) with the light curves of these new variables. Most of these sources will also fall into the TESS footprint, thus short baseline

TESS light curves that possess better photometric precision can also be obtained to complement the long baseline ASAS-SN light curves.

This work greatly improves the completeness of bright variables in the Southern hemisphere and provides long baseline *V*-band light curves. In particular, we have significantly improved the completeness of lower amplitude variables. As part of our ongoing effort to systematically analyse all the ~ 50 million $V < 17$ mag APASS sources for variability, we will next update this database with the light curves for the sources across the Northern hemisphere and include the light curves for sources missing from the APASS DR9 catalogue.

REFERENCES

Alard C., 2000, A&AS, 144, 363
Alard C., Lupton R. H., 1998, ApJ, 503, 325

Alcock C. et al., 1997, ApJ, 486, 697
Astropy Collaborationet al.2013, A&A, 558, A33
Bailer-Jones C. A. L., Rybizki J., Fouesneau M., Mantelet G., Andrae R., 2018, AJ, 156, 58
Beaton R. L. et al., 2018, Space Sci. Rev., 214, 113
Bhatti W. et al., 2018, astrobase, v0.3.8, Zenodo, doi:10.5281/zenodo.1185231
Breger M., 1979, PASP, 91, 5
Breiman L., 2001, Mach. Learn., 45, 1
Brown T. M. et al., 2013, PASP, 125, 1031
Chen X., Wang S., Deng L., de Grijs R., Yang M., 2018, ApJS, 237, 28
Clarke D., 2002, A&A, 386, 763
Cutri R. M. et al., 2013, VizieR Online Data Catalog, 2328
Derue F. et al., 2002, A&A, 389, 149
Drake A. J. et al., 2014, ApJS, 213, 9
Feast M., Whitelock P. A., 2014, Setting the Scene for Gaia and LAMOST, Cambridge University Press, Cambridge, p. 40
Fernández-Trincado J. G., Vivas A. K., Mateu C. E., Zinn R., Robin A. C., Valenzuela O., Moreno E., Pichardo B., 2015, A&A, 574, A15
Gaia Collaboration et al., 2018a, A&A, 616, A1
Gaia Collaboration et al., 2018b, A&A, 623, A110
Gaia Collaboration et al., 2018c, A&A, 616, A12
Graczyk D. et al., 2014, ApJ, 780, 59
Heinze A. N. et al., 2018, AJ, 156, 241
Henden A. A., Levine S., Terrell D., Welch D. L., 2015, American Astronomical Society Meeting Abstracts #225, 225, 336.16
Holl B. et al., 2018, A&A, 618, A30
Holoien T. W.-S. et al., 2014, MNRAS, 445, 3263
Holoien T. W.-S. et al., 2016, MNRAS, 455, 2918
Holoien T. W.-S. et al., 2017, MNRAS, 471, 4966
Holoien T. W.-S. et al., 2018a, , MNRAS, 484, 1899
Holoien T. W.-S. et al., 2018b, ApJ, 880, 120
Holtzman J. A. et al., 2015, AJ, 150, 148
Jayasinghe T. et al., 2018a, MNRAS, 477, 3145
Jayasinghe T. et al., 2018b, Res. Notes Am. Astron. Soc., 2, 181
Jayasinghe T. et al., 2018c, Res. Notes Am. Astron. Soc., 2, 125
Jayasinghe T., Stanek K. Z., Kochanek C. S., Thompson T. A., Shappee B. J., Fausnaugh M., 2018d, MNRAS, 489, 4705
Jayasinghe T. et al., 2019a, MNRAS, 486, 1907
Jayasinghe T. et al., 2019b, MNRAS, 485, 961
Jayasinghe T. et al., 2019c, Astron. Telegram, 12836, 1
Kim D.-W., Bailer-Jones C. A. L., 2016, A&A, 587, A18
Kochanek C. S. et al., 2017, PASP, 129, 104502
Kovács G., Zucker S., Mazeh T., 2002, A&A, 391, 369
Lafler J., Kinman T. D., 1965, ApJS, 11, 216
Leavitt H. S., 1908, Ann. Harv. Coll. Obs., 60, 87
Lebzelter T., Mowlavi N., Marigo P., Pastorelli G., Trabucchi M., Wood P. R., Lecoeur-Taibi I., 2018, A&A, 616, L13
Liao S.-L., Qi Z.-X., Guo S.-F., Cao Z.-H., 2019, Res. Astron. Astrophys., 19, 029

Lopez de Coca P., Rolland A., Rodriguez E., Garrido R., 1990, A&AS, 83, 51
Madore B. F., 1982, ApJ, 253, 575
Marrese P. M., Marinoni S., Fabrizio M., Altavilla G., 2019, A&A, 621, A144
Mateu C., Vivas A. K., 2018, MNRAS, 479, 211
Mateu C., Vivas A. K., Downes J. J., Briceno C., Zinn R., Cruz-Diaz G., 2012, MNRAS, 427, 3374
Matsunaga N., 2018, Rediscovering Our Galaxy, Cambridge University Press, Cambridge, p. 57
Matsunaga N. et al., 2006, MNRAS, 370, 1979
McDonald I., De Beck E., Zijlstra A. A., Lagadec E., 2018, MNRAS, 481, 4984
Oelkers R. J. et al., 2018, AJ, 155, 39
Pawlak M. et al., 2016, Acta Astron., 66, 421
Pawlak M. et al., 2019, MNRAS, 487, 5932
Pedregosa F. et al., 2012, preprint (arXiv:1201.0490)
Percy J. R., Fenaux L., 2019, preprint (arXiv:1905.03279)
Pojmanski G., 2002, Acta Astron., 52, 397
Ricker G. R. et al., 2015, J. Astron. Telesc. Instrum. Syst., 1, 014003
Scargle J. D., 1982, ApJ, 263, 835
Shappee B. J. et al., 2014, ApJ, 788, 48
Shields J. V. et al., 2018, MNRAS, 483, 4470
Skrutskie M. F. et al., 2006, AJ, 131, 1163
Soszynski I. et al., 2005, Acta Astron., 55, 331
Soszyński I. et al., 2016, Acta Astron., 66, 405
Taylor M. B., 2005, in Shopbell P., Britton M., Ebert R., eds. ASP Conf. Ser. Vol. 347, Astronomical Data Analysis Software and Systems XIV. Astron. Soc. Pac.. San Francisco, p. 29
Thompson T. A. et al., 2018, preprint (arXiv:1806.02751)
Tonry J. L. et al., 2018a, PASP, 130, 064505
Tonry J. L. et al., 2018b, ApJ, 867, 105
Torres G., Andersen J., Giménez A., 2010, A&AR, 18, 67
Udalski A., 2003, Acta Astron., 53, 291
Udalski A. et al., 2018, Acta Astron., 68, 315
VanderPlas J. T., 2018, ApJS, 236, 16
Von Neumann J., Kent R., Bellinson H., Hart B. T., 1941, Ann. Math. Stat., 12, 153
Watson C. L., Henden A. A., Price A., 2006, in Society for Astronomical Sciences 25th Annual Symposium on Telescope Science. Society for Astronomical Sciences, p. 47
Whitelock P. A., Feast M. W., Van Leeuwen F., 2008, MNRAS, 386, 313
Woźniak P. R. et al., 2004, AJ, 127, 2436
Wright E. L. et al., 2010, AJ, 140, 1868
Zechmeister M., Kürster M., 2009, A&A, 496, 577

This paper has been typeset from a TEX/LATEX file prepared by the author.